Three-dimensional optical tomography: resolution in small-object imaging

Hamid Dehghani, Brian W. Pogue, Jiang Shudong, Ben Brooksby, and Keith D. Paulsen

Near-infrared (NIR) optical tomography can provide estimates of the internal distribution of optical absorption and transport scattering from boundary measurements of light propagation within biological tissue. Although this is a truly three-dimensional (3D) imaging problem, most research to date has concentrated on two-dimensional modeling and image reconstruction. More recently, 3D imaging algorithms are demonstrating better estimation of the light propagation within the imaging region and are providing the basis of more accurate image reconstruction algorithms. As 3D methods emerge, it will become increasingly important to evaluate their resolution, contrast, and localization of optical property heterogeneity. We present a concise study of 3D reconstructed resolution of a small, low-contrast, absorbing and scattering anomaly as it is placed in different locations within a cylindrical phantom. The object is an 8-mm-diameter cylinder, which represents a typical small target that needs to be resolved in NIR mammographic imaging. The best resolution and contrast is observed when the object is located near the periphery of the imaging region (12–22 mm from the edge) and is also positioned within the multiple measurement planes, with the most accurate results seen for the scatter image when the anomaly is at 17 mm from the edge. Furthermore, the accuracy of quantitative imaging is increased to almost 100% of the target values when *a priori* information regarding the internal structure of imaging domain is utilized.

OCIS codes: 170.3010, 110.6880.

1. Introduction

Near-infrared (NIR) optical tomography is a three-dimensional (3D) imaging method that can reconstruct physiologically relevant chromophore distributions from the region under investigation.[1–7] Light is transmitted through tissue by means of multiple input and output locations, similar to that in a fan-beam, x-ray computed tomography geometry, but with optical fibers for delivery and pickup of the light signals. The intensity and path-length distributions of the exiting photons provide information about the optical properties of the transilluminated tissue by means of a model-based interpretation in which photon propagation is simulated by diffusion theory. Through iterative solution matching of the theoretical prediction to the actual measured values, images of internal absorption and scattering coefficient distribution can be reconstructed. The main interest in this study lies in the ability to detect and characterize tumors within the female breast.[1,2] Since the absorption and scattering of light in tissue is a function of its optical properties, and hence its physiological state, our aim is to obtain images of internal optical absorption μ_a, reduced scattering μ_s', and ultimately of total hemoglobin and oxygen saturation distributions. These images should, in principle, provide information about the physiological state of the tissue under investigation and help identify and characterize tumors within the breast.

Despite evidence of high contrast, NIR imaging is confounded by a dominant scattering, which serves to limit its spatial resolution. Light is attenuated similarly for both absorption and scattering heterogeneities, making quantitative absorption imaging a challenging task. The use of frequency-domain and time-resolved techniques to obtain path-length information, in combination with model-based iterative reconstruction methods, allows for the separation of absorption and scattering heterogeneities[8] and improves spatial resolution and contrast.[9] However, as with all imaging systems, there is a trade-off be-

The authors are with Thayer School of Engineering, Dartmouth College, Hanover, New Hampshire 03755. H. Dehghani's e-mail address is hamid.dehghani@dartmouth.edu.

Received 30 August 2002; revised manuscript received 3 December 2002.

0003-6935/03/163117-12$15.00/0

tween spatial resolution and contrast recovered, and diffusion tomography has its own response curve.[10] As objects become smaller, the contrast required for accurate recovery becomes higher. For breast imaging this trade-off is important to characterize because the required resolution for a given contrast can be determined from clinically derived estimates of breast cancers.

Most modeling and image reconstruction studies have involved two-dimensional (2D) assumptions, yet a 3D treatment of light propagation in tissue provides a more accurate prediction of the fluence distribution in the medium. Recently there has been significant progress in developing 3D modeling and image reconstruction,[1–4,11–13] which is computationally more complex but also more accurate. As 3D image reconstruction becomes more fully developed, it is crucial to define the resolution and the contrast available from these algorithms analogously to the studies that have been completed in two dimensions.[10] This requirement is particularly true when experimental data is used, since theoretical simulations typically do not represent the level of noise and systematic error present in actual data sets. Indeed, our studies have shown that it is the systematic errors that limit 2D diffusion tomography and ultimately constrain the resolution and contrast that can be recovered.[14,15] Most studies have shown that although images of optical absorption and scatter can be reconstructed simultaneously, the quantitative accuracy of these quantities remains relatively poor.

In this research, a series of phantom studies was completed with an automated clinical prototype frequency-modulated NIR breast tomography system.[16] Data from a phantom containing a single anomaly with a higher absorption and scatter relative to the background was acquired. The object was moved laterally and vertically through the phantom to evaluate the 3D field response. The accuracy of the reconstruction in both resolution and localization of the anomaly was tested with an improved 3D algorithm.[2] Although the spatial resolution and contrast derived is limited in this case, the use of *a priori* information about the object location and size provides the vehicle for accurately quantifying the true absorption and scattering coefficients. This use of *a priori* information represents the first demonstration of accurate absolute quantification of absorption and scattering coefficients by use of a 3D algorithm with measured data for image reconstruction with NIR tomography, although previous research in fluorescent tomography has also been reported.[17]

2. Theory

Under the assumption that scattering dominates absorption in a region of interest, the Boltzmann transport equation can be simplified to the diffusion approximation, which in the frequency domain is given by

$$-\nabla \cdot \kappa(r)\nabla\Phi(r, \omega) + \left(\mu_a + \frac{i\omega}{c}\right)\Phi(r, \omega) = q_0(r, \omega), \tag{1}$$

where $q_0(r, \omega)$ is an isotropic source, $\Phi(r, \omega)$ is the photon fluence rate at position $\boldsymbol{r}$, and $\kappa = 1/[3(\mu_a + \mu_s')]$ is the diffusion coefficient. We use the Robin-type (type III) boundary condition

$$\Phi(\gamma) + \frac{\kappa}{\alpha}\hat{n} \cdot \nabla\Phi(\gamma) = 0, \tag{2}$$

where α is a term that incorporates reflection as a result of refractive-index mismatch[18] at the boundary, and $\hat{n}$ is the outward pointing normal to the boundary ($\delta\Omega$) at γ.

We assume that the data is represented by a nonlinear operator $y^* = F(\mu_a, \kappa)$, where our data y^* is a complex vector having real and imaginary components, which are mapped to log amplitude and phase in measurement. Then the image reconstruction method seeks a solution,

$$(\hat{\mu}_a, \hat{\kappa}) = \arg\min_{\mu_a,\kappa} \| [y^* - F(\mu_a, \kappa)] \|, \tag{3}$$

where $\|.\|$ is the weighted L2-norm, representing the square root of the sum of the squared elements. The magnitude of this weighted L2-norm is sometimes referred to as the projection error and provides a value for determining the convergence of the iterative reconstruction algorithm.

We use a finite-element method as a general and flexible method for solving the forward problem in arbitrary geometries.[19,20] In the inverse problem, where we aim to recover internal optical property distributions from boundary measurements, we assume that $\mu_a(\mathbf{r})$ and $\kappa(\mathbf{r})$ are expressed in a basis with a limited number of dimensions (less than the dimension of the finite-element system matrices). Numerous different strategies for defining reconstruction bases are possible; in this paper we use a second mesh basis,[21] whose local shape and continuity characteristics are the same as the original mesh, but with fewer degrees of freedom. To find $(\hat{\mu}_a, \hat{\kappa})$ in Eq. (3) we have used a Levenberg–Marquardt algorithm, where we repeatedly solve

$$a = J^T(JJ^T + \rho I)^{-1}b, \tag{4}$$

where $\mathbf{b}$ is the data vector, $b = [y^* - F(\mu_a, \kappa)]^T$, and $\mathbf{a}$ is the solution update vector, $a = (\delta\kappa; \delta\mu_a)$. Variable ρ is the regularization factor, and J is the Jacobian matrix for our model, which is calculated with the Adjoint method.[22] Equation (4) is known as the Moore–Penrose generalized inverse and is found to be highly suitable to 3D problems for which the number of unknowns to be recovered is much

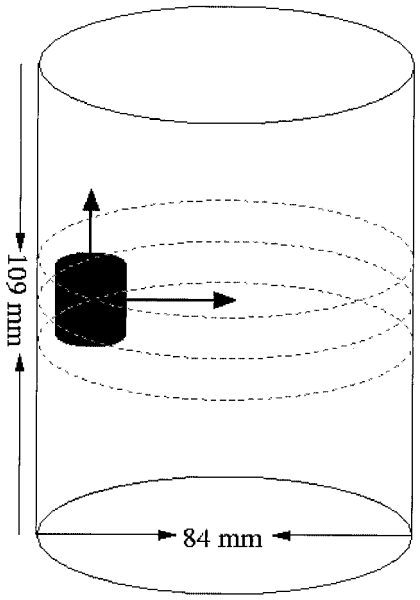

Fig. 1. Schematic diagram of the experimental setup in which a hollow phantom of radius 42 mm and of height 109 mm was filled with a mixture of Intralipid solution and India ink to produce a uniform background $\mu_a = 0.0058\ \text{mm}^{-1}$ and $\mu_s' = 1.26\ \text{mm}^{-1}$. The small cylindrical anomaly had a radius of 8 mm and a height of 10 mm with $\mu_a = 0.0099\ \text{mm}^{-1}$ and $\mu_s' = 1.5\ \text{mm}^{-1}$. The anomaly was initially positioned at $x = -27$ mm, $y = 0$ mm, and $z = 0$ mm. The dashed curves represent the measurement planes, at $z = -10$ mm, $z = 0$ mm, and $z = 10$ mm, each containing 16 source–detector fibers, starting with the bottom curve.

larger than the amount of information (measurements) available, which is the case in an underdetermined problem.[2,23]

3. Experiment

The research presented in the following section is based on data measured from a phantom in which our frequency-domain NIR system was used. A hollow phantom of radius 42 mm and height 109 mm was filled with a mixture of Intralipid solution and India ink to produce a uniform background $\mu_a = 0.0058\ \text{mm}^{-1}$ and $\mu_s' = 1.26\ \text{mm}^{-1}$. Within this phantom a small cylindrical object of radius 8 mm and height 10 mm with optical properties of $\mu_a = 0.0099\ \text{mm}^{-1}$ and $\mu_s' = 1.5\ \text{mm}^{-1}$ was suspended as illustrated schematically in Fig. 1. In this figure, the dashed curves represent the planes of measurement, 10 mm apart at z of -10, 0, and 10 mm with 16 sources and measurement sites per plane. Data were collected at 100 MHz with a 785-nm light source. In addition, a set of data was measured without the anomaly present to allow calibration based on the procedure described in Refs. 2 and 16.

Use of Eq. (4) allowed 3D images of internal optical properties to be calculated from these measurements. The finite-element mesh used to calculate the Jacobian was a cylindrical mesh of radius 42 mm and height of 109 mm [Fig. 2(a)]. It contained 9,211 nodes corresponding to 45,980 linear tetrahedral elements.[24] For the reconstruction basis, another mesh was used

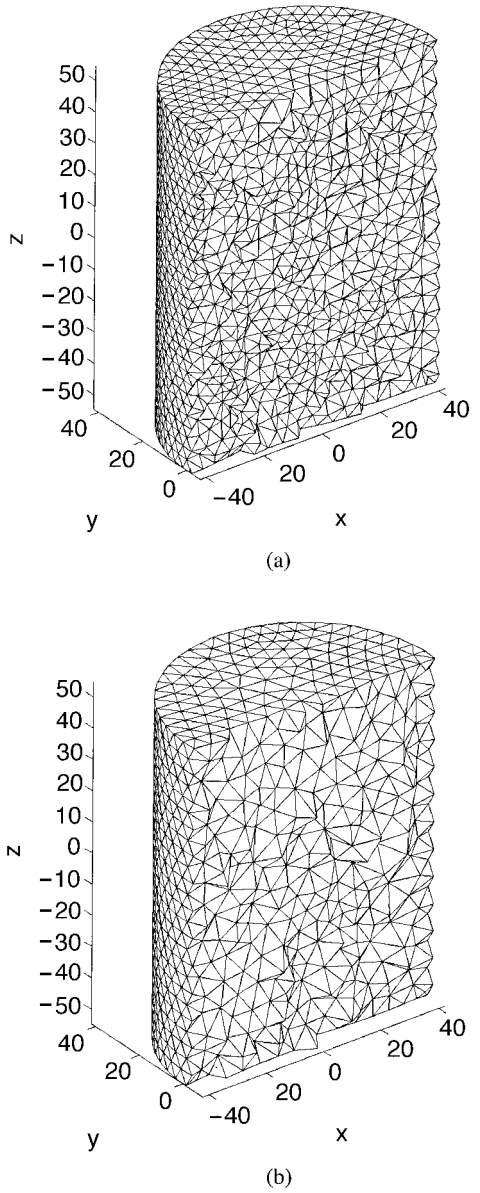

Fig. 2. Finite-element, 3D meshes used for modeling and image reconstruction. Mesh used for calculation of (a) the Jacobian and (b) the lower-resolution reconstruction mesh. In both cases, cross sections through the plane defined by $y = 0$ mm are shown.

that was of the same geometry but contained 3,718 nodes corresponding to 16,627 linear tetrahedral elements [Fig. 2(b)]. The regularization parameter, ρ, was initially set to 10 and was varied at each iteration by a factor of $10^{1/4}$ if the projection error [Eq. (3)] was less than the previous iteration. If the projection error was found to increase, ρ increased by a factor of $10^{1/8}$. The results shown in Section 4 represent the twentieth iteration of the reconstruction algorithm. The reconstruction time, after the initial calibration procedure, was approximately 20 min per iteration on a 1.7-GHz PC with 2 Gb of RAM. The twentieth iteration was chosen as a suitable stopping point because the projection error did not decrease more than 1% relative to the previous iteration.

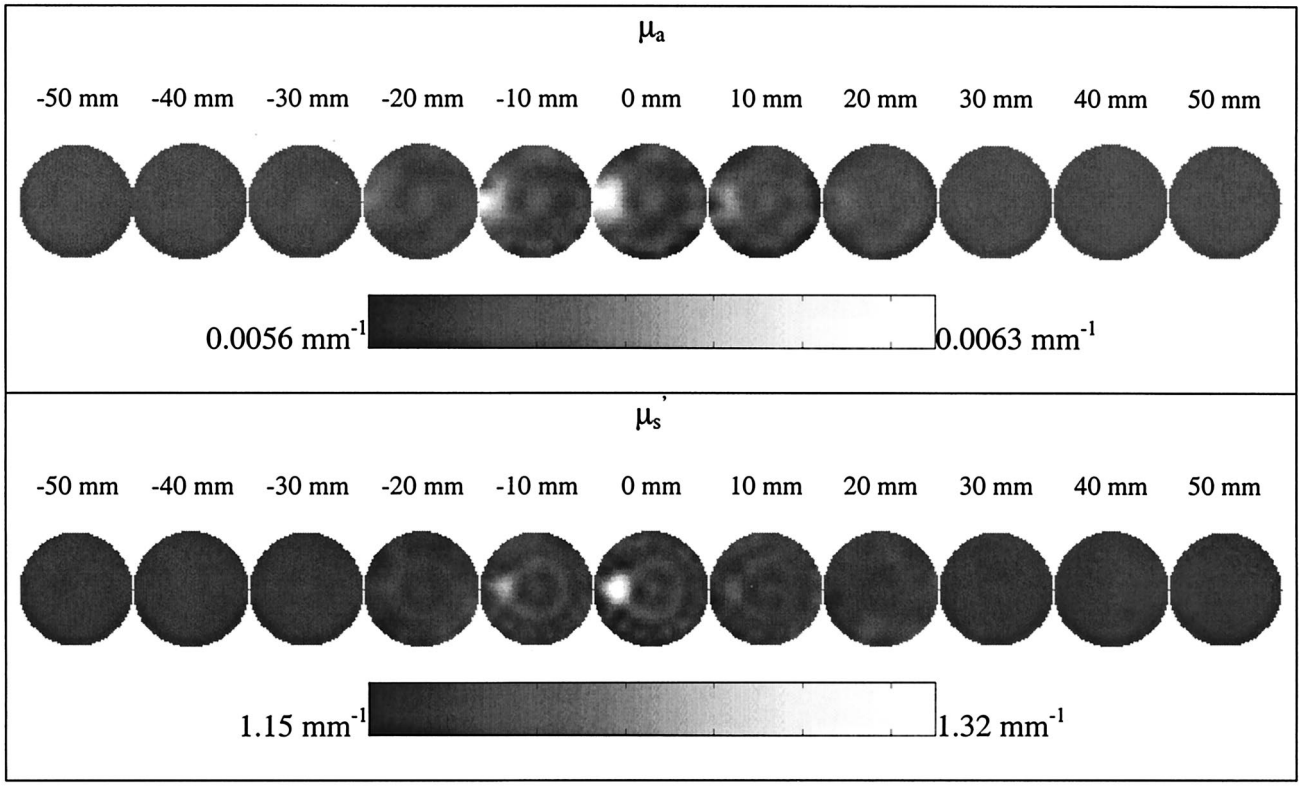

Fig. 3. Reconstructed images when the anomaly is located at $x = -27$ mm, $y = 0$ mm, and $z = 0$ mm. The top row contains absorption images, and the bottom row shows the reduced scatter images. In each case, images are 2D cross sections through the reconstructed 3D volume. The right-hand side corresponds to the top of the cylinder ($z = 50$ mm), whereas the left corresponds to the bottom of the cylinder ($z = -50$ mm), with each slice representing a 10-mm increment.

4. Results

A. Mid-Plane Resolution

The cylindrical anomaly was positioned at $x = -27$ mm, $y = 0$ mm, and $z = 0$ mm, and data were collected in all three measurement planes, as shown in Figure 1. The anomaly was then moved radially inwards at 5-mm increments, and new sets of data were collected until the anomaly reached a position of $x = -2$ mm. From each set of data as the anomaly was radially moved inwards, 3D images were reconstructed: these images are shown in Figs. 3–8. In each of these figures, the top row corresponds to μ_a images, and the bottom row corresponds to μ_s' images. These are 2D cross sections through the reconstructed 3D images. The right-hand side corresponds to the top of the cylinder ($z = 50$ mm), and the left corresponds to the bottom of the cylinder ($z = -50$ mm), with each slice corresponding to a 10-mm increment.

From this series of reconstructed images it can be seen that the anomaly has been reconstructed in the correct plane ($z = 0$ mm), at approximately the right position. The most striking result from these reconstructed images is that the absolute values of the optical properties of the anomaly are only approximately 10% of the expected values. Methods for increasing accuracy are discussed and demonstrated in Subsection 4C.

For a more quantitative assessment of these results, transects of both μ_a and μ_s' reconstructed values, at $z = 0$ mm and $y = 0$ mm, are plotted in Figs. 9(a) and 9(b), respectively. From these graphs, it is possible to calculate the peak position for each set of the data, as well as the full width half-maximum (FWHM) of the anomaly at each position. The FWHM was computed as the width at half the maximum value, with respect to the mean throughout the image. These values are reported in Table 1. From these calculated values, it is evident that regardless of the actual position of the anomaly, the peak position of the reconstructed anomaly is within 1–7 mm of its true location, with the μ_s' reconstruction showing the best accuracy. The μ_a image of the anomaly near the edge of the phantom has the most artifact, which is because of its proximity to the inner edge of the hollow phantom. From the calculated FWHM of the anomaly, it is clear that as the object is moved further toward the center of the phantom, it appears larger. The calculated μ_s' FWHM exhibits more variation but is much sharper and better defined in terms of the actual object size. The peak values of the anomaly, as shown in Figs. 9(a) and 9(b), also decrease as the object is moved toward the center of the hollow phantom and never quite reaches the true absorption coefficient of 0.0099 mm^{-1}.

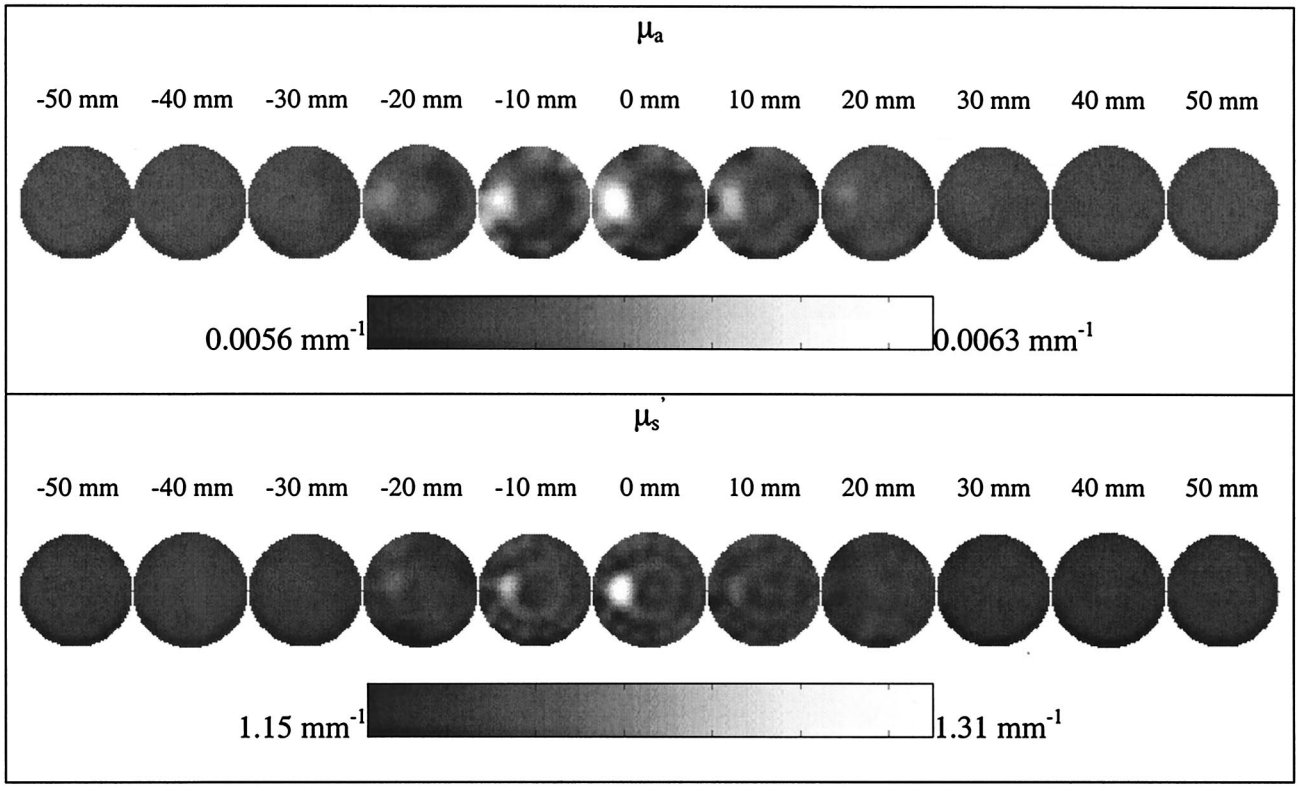

Fig. 4. Same as Fig. 3, with the anomaly at $x = -22$ mm.

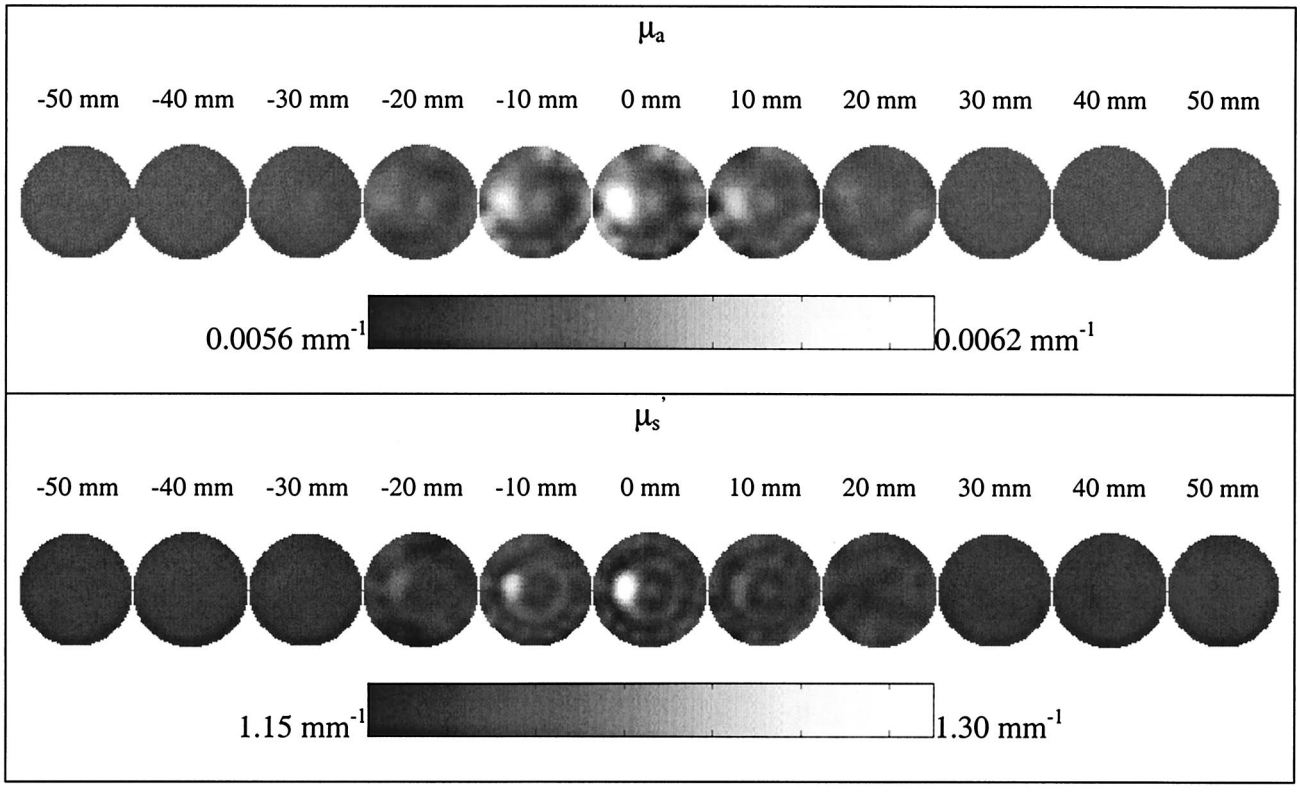

Fig. 5. Same as Fig. 3, with the anomaly at $x = -17$ mm.

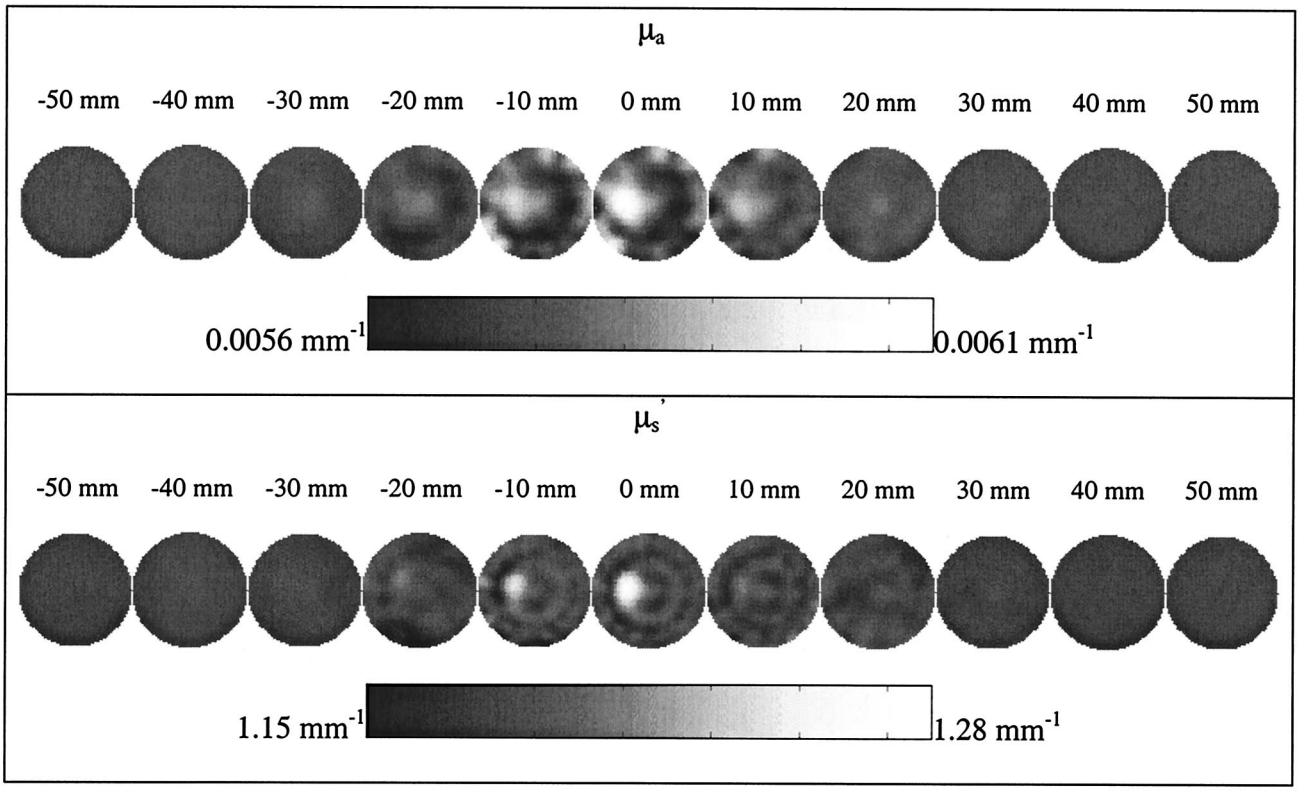

Fig. 6. Same as Fig. 3, with the anomaly at $x = -12$ mm.

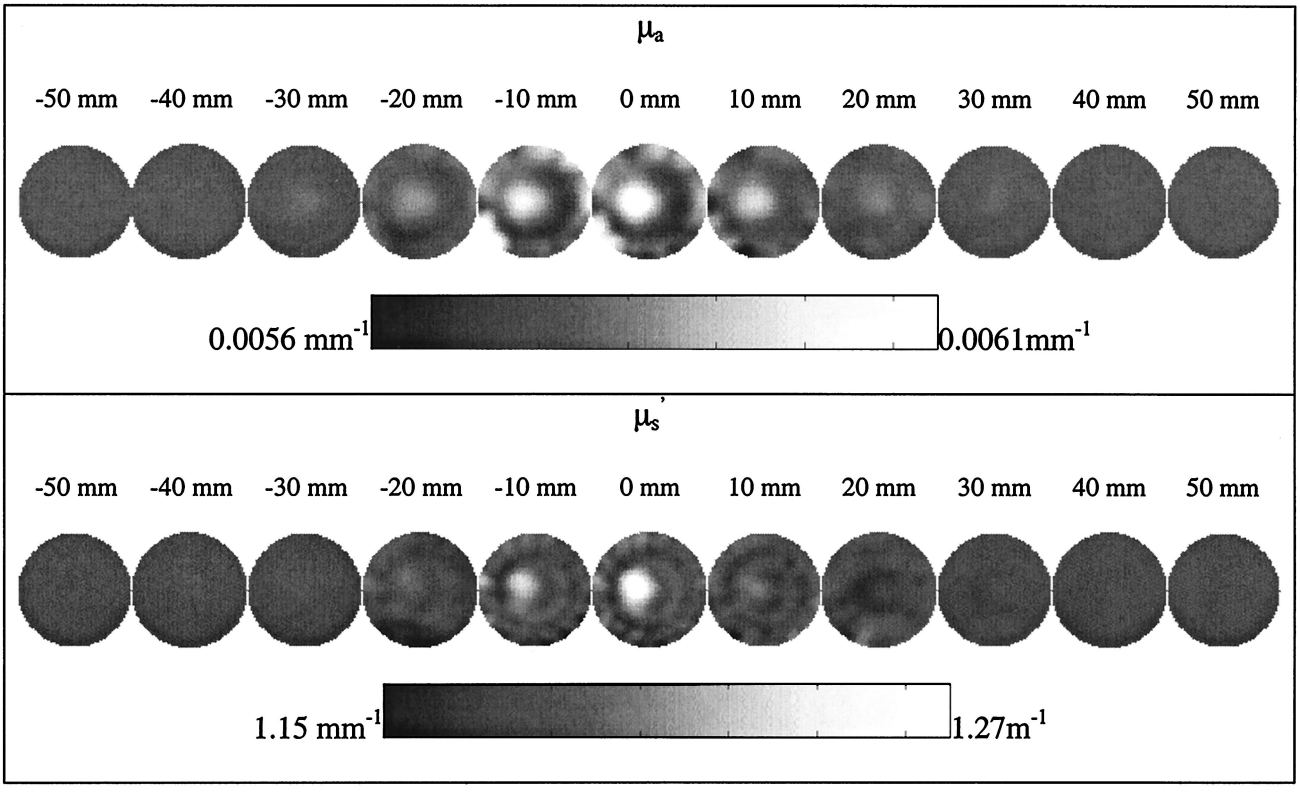

Fig. 7. Same as Fig. 3, with the anomaly at $x = -7$ mm.

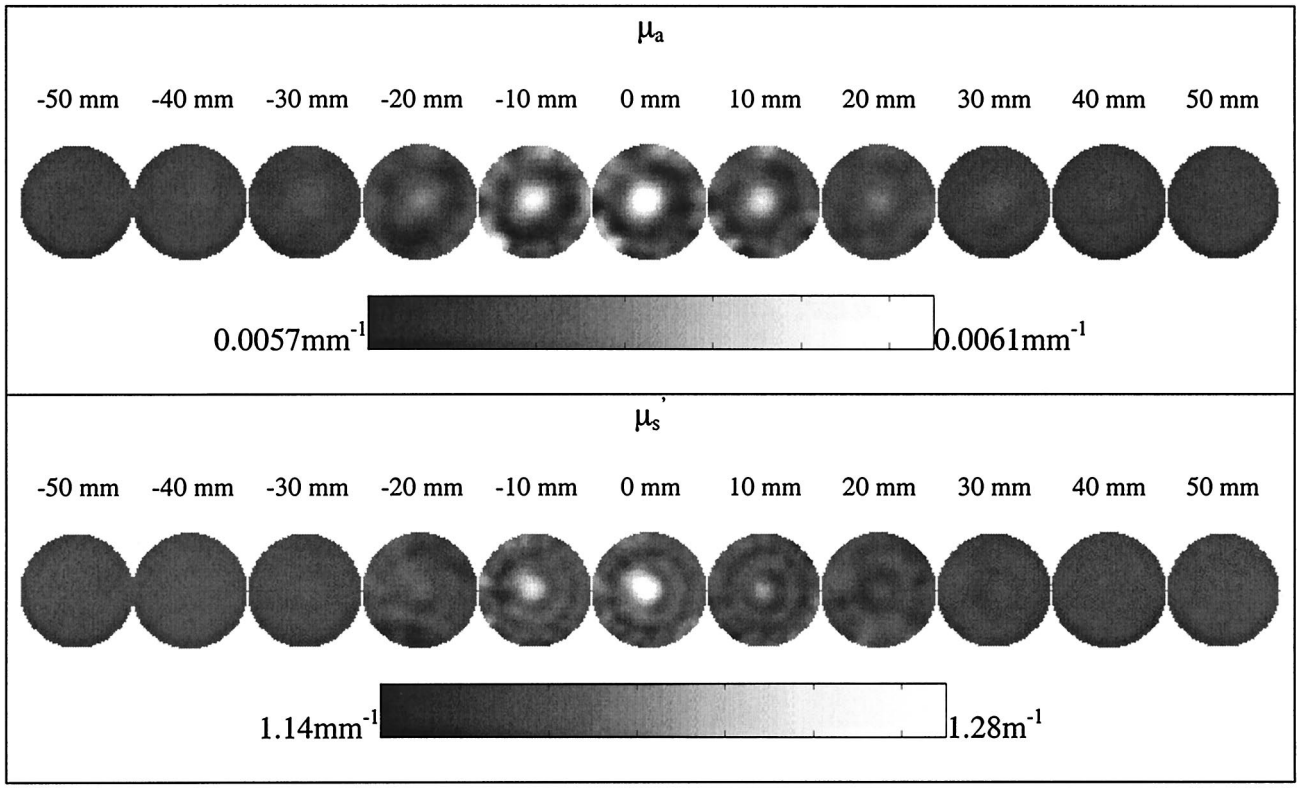

Fig. 8. Same as Fig. 3, with the anomaly at $x = -2$ mm.

B. Out-of-Plane Resolution

The cylindrical anomaly was positioned at $x = -22$ mm, $y = 0$ mm, and $z = 20$ mm, and data were collected in all three measurement planes. The anomaly was then moved vertically downward to $z = 10$ mm, and new sets of data were collected. The 3D reconstructed images from these experiments are shown in Figs. 10 and 11, for $z = 20$ mm and $z = 10$ mm, respectively. For cross comparison, the object at $z = 0$ mm is shown in Fig. 4.

From Figs. 10 and 11, it is again evident that the anomaly has been reconstructed accurately in position; the peak value appears in the correct plane although with decreased overall contrast as before. Transects both μ_a and μ_s' at $x = -20$ mm and $y = 0$ mm are plotted in Figs. 12(a) and 12(b), respectively. From these plots, it can be seen that the scatter image recovers the position of the anomaly better than the absorption images. The largest error occurs when the anomaly is located at $z = 20$ mm, which is 10 mm above the upper measurement plane. Again, the actual reconstructed values are lower than expected.

C. Use of *A Priori* Information

The reconstructed images presented in Subsections 4A and 4B have shown accurate recovery of the location of the anomaly, but the absolute values of the estimated optical properties are relatively poor. There are several reasons for this, including the large underdetermined nature of the problem and the partial volume effect.[13] Methods exist that can assist in better image reconstruction, and possibly the most applicable solution is the use of *a priori* information.[25] For demonstration purposes we have taken the data collected when the anomaly is positioned at $x = -22$ mm, $y = 0$ mm, and $z = 0$ mm. Using *a priori* information about the position and size of the anomaly, we created a mesh incorporating the object as shown in Fig. 13. For the reconstruction, we used this *a priori* information to create two regions within the mesh: background and object.

We segment our mesh (Fig. 13) by assigning all nodes within each region with the appropriate labels (background = 0, object = 1). In general, given structural segmentation into n regions, we reconstruct for single values of μ_a and μ_s' within each region. We apply a matrix transformation to J, such that

$$\tilde{J} = JK, \tag{5}$$

where the dimensions of $\tilde{J}$ are number of measurements by number of regions (NM × NR). We call K the *a priori* matrix

$$K = \begin{bmatrix} R_1 & R_2 & \Lambda & R_n \\ k_{1,1} & k_{1,2} & \Lambda & k_{1,n} \\ k_{2,1} & k_{2,2} & \Lambda & k_{2,n} \\ \mathrm{M} & \mathrm{M} & \mathrm{O} & \mathrm{M} \\ k_{j,1} & k_{j,2} & \Lambda & k_{j,n} \end{bmatrix},$$

$$\text{where } k_{\xi,\eta} = \begin{Bmatrix} 1, & \xi \in R_\eta \\ 0, & \xi \notin R_\eta \end{Bmatrix}. \tag{6}$$

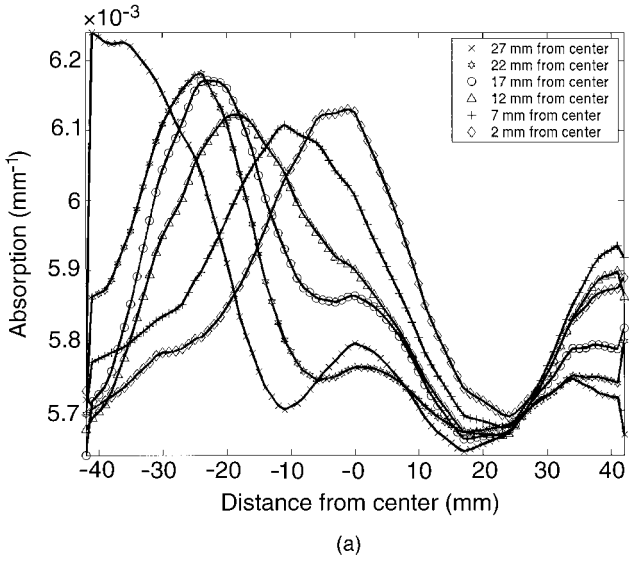

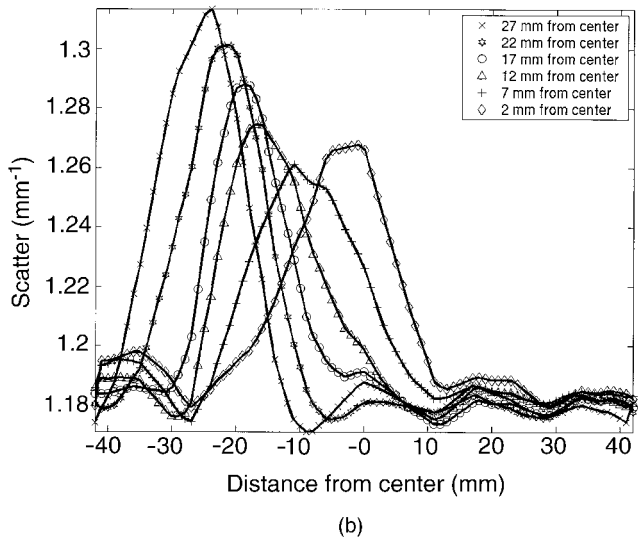

Fig. 9. Calculated transects of both (a) μ_a and (b) μ_s' at $z = 0$ mm and $y = 0$ mm for images shown in Figs. 3–8.

In effect, we produce a new Jacobian matrix, $\tilde{J}$, in which we have added together all elements from the columns corresponding to like regions. We then solve

$$\tilde{\mathbf{a}} = (\tilde{J}^T\tilde{J})^{-1}\tilde{J}^T b, \tag{7}$$

where the dimensions of the solution update vector, $\tilde{\mathbf{a}}$, are $2 \times$ NR. In the update process, we apply

$$a = \tilde{a}K^{-1}. \tag{8}$$

Note that regularization is not required in solving matrix Eq. (7) because NR $\ll$ NM, and therefore the Hessian is a small, well-conditioned matrix.

Images were reconstructed with the data with Eq. (7), and the results at the twentieth iteration are shown in Fig. 14. It can be seen from these results that since we perform regional reconstruction, the calculated values within each zone are homogenous.

Table 1. Calculated Peak and FWHM of the Absorption and Transport Scattering Values for the Reconstructed Images Shown in Figs. 3–8

	Peak		FWHM	
Radial Distance (mm)	μ_a (mm)	μ_s' (mm)	μ_a (mm)	μ_s' (mm)
2	1	1	18.02	14.41
7	11	11	18.41	16.9
12	19	17	18	12.85
17	23	19	17.41	11.64
22	24	21	16.5	12.5
27	41	24	18.65	13.5

Furthermore, it is evident that the absolute reconstructed values are accurate (3% error for the absorption image and 6.6% for the scatter image).

5. Discussion

In this research we have presented initial results for the determination of image resolution and anomaly localization for 3D NIR optical tomography. We have collected 3D data using our frequency-domain system from a hollow phantom containing a homogenous Intralipid solution of known optical properties in the presence of a single anomaly that had higher absorption and scatter relative to the background. The object was initially placed within the mid plane of the detection array ($z = 0$ mm) near the edge of the phantom ($x = -27$ mm), and a full set of data was collected. The object was then moved radially inwards toward the center of the phantom at 6 discrete steps of 5 mm, and new sets of data were collected. From the measured data, 3D images of absorption and scatter were reconstructed simultaneously and presented in Figs. 3–8.

The reconstructed images have shown good accuracy in the localization of the anomaly, however the absolute quantitative accuracy in the estimated optical properties is not good. There are several reasons for this:

1. the anomaly is a small object (radius 8 mm, height 10 mm) and has a low contrast in both absorption (2 times background) and scatter (1.5 times background),
2. the image reconstruction is highly underdetermined; there are 1440 measurements (720 log amplitude and 720 phase measurements) compared with 7436 (3718×2) unknowns.

Despite the low quantitative accuracy, the localization of the anomaly is within 7 mm of the true position in the worst case (in which the object is 12 mm from center).

Transect plots through the plane of interest ($z = 0$ mm) are shown in Figs. 9(a) and 9(b) for the absorption and scatter images, respectively. These graphs show that the peak value of the reconstructed anomaly moves inwards as the object is moved inwards toward the center of the phantom. The measured

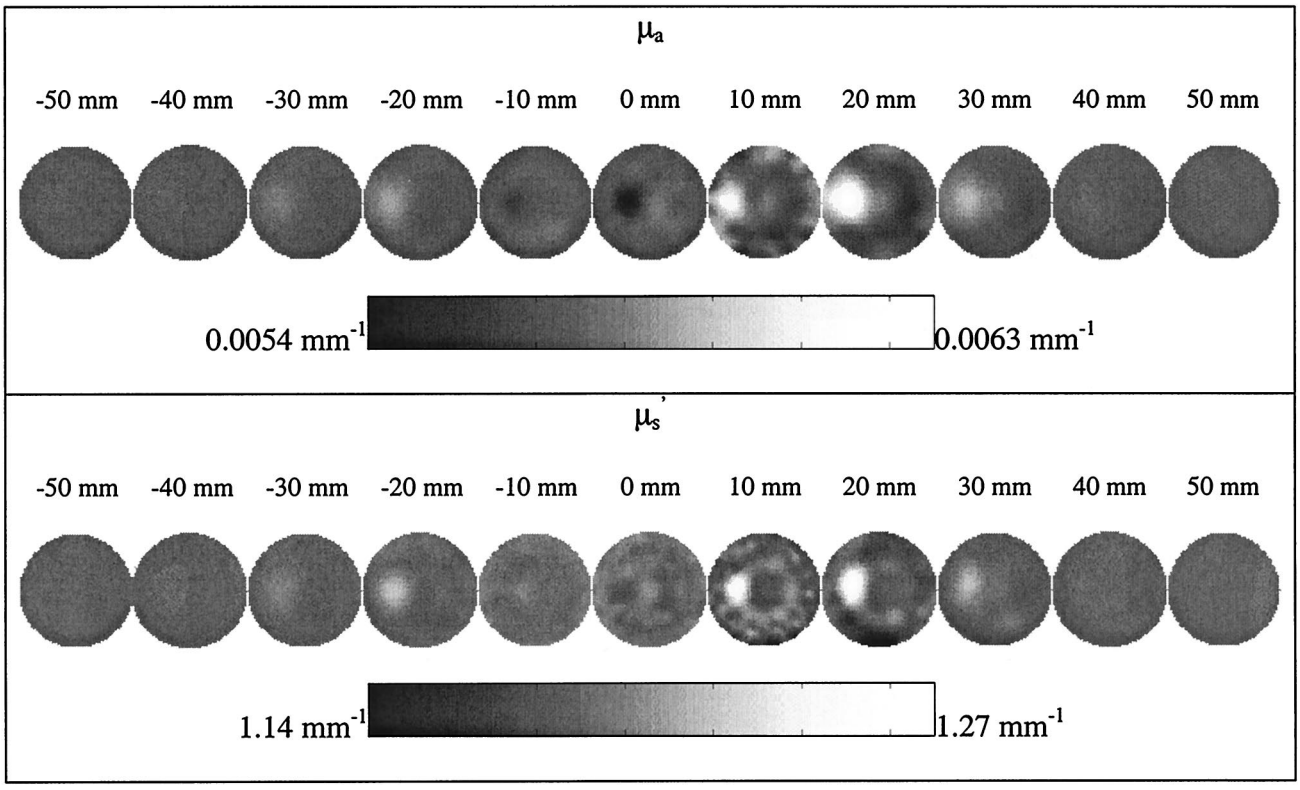

Fig. 10. Reconstructed images when the anomaly is located at $x = -22$ mm, $y = 0$ mm, and $z = 20$ mm. Top row is absorption coefficient images, whereas those in the bottom row are reduced scattering coefficient images. Displayed are 2D cross sections through the reconstructed 3D volume. The right-hand side corresponds to the top of the cylinder ($z = 50$ mm), and the left corresponds to the bottom of the cylinder ($z = -50$ mm), with each slice being a 10-mm increment.

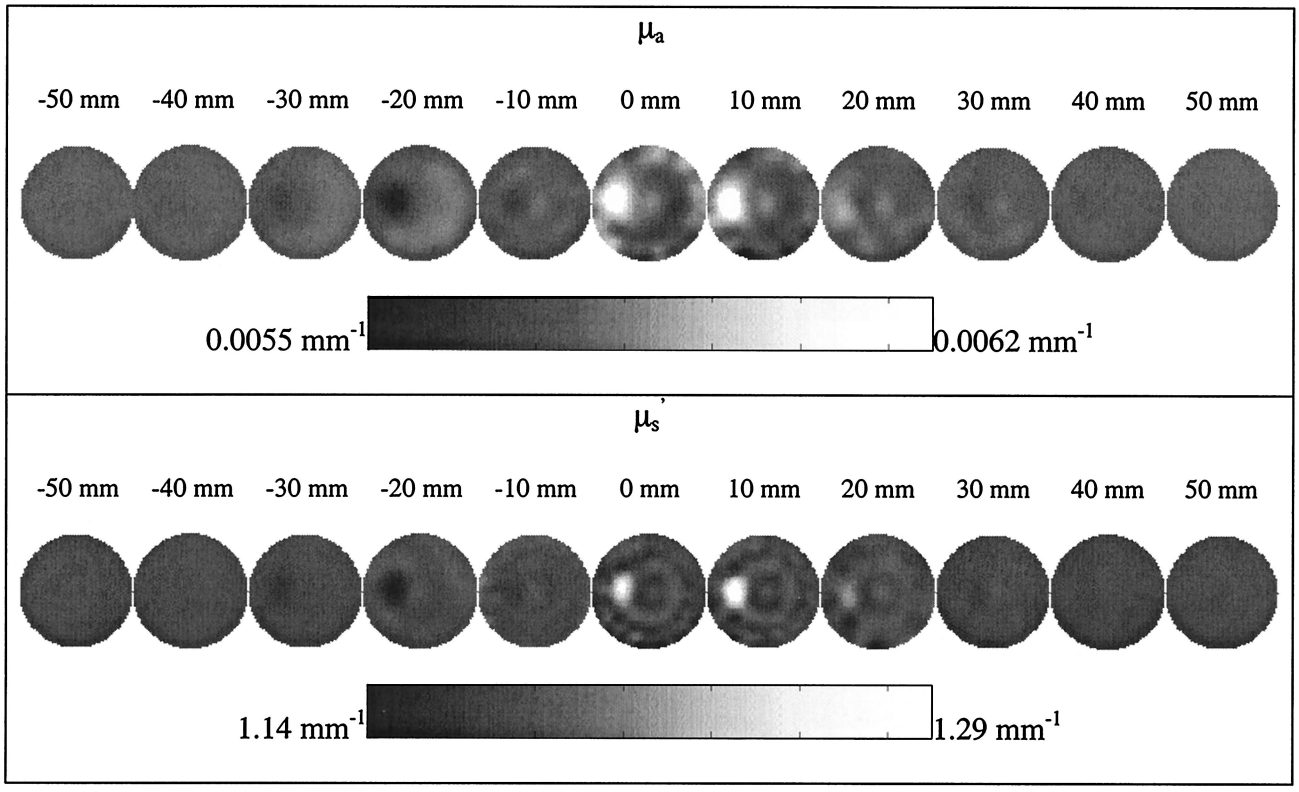

Fig. 11. Same as Fig. 10, with the anomaly positioned at $x = -22$ mm, $y = 0$ mm, and $z = 10$ mm.

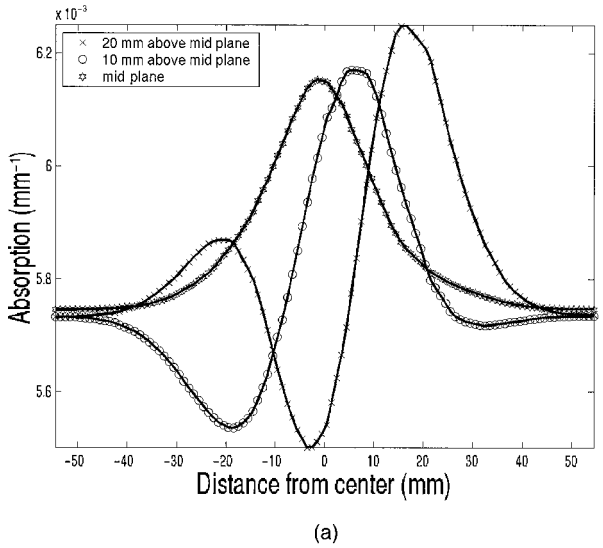

(a)

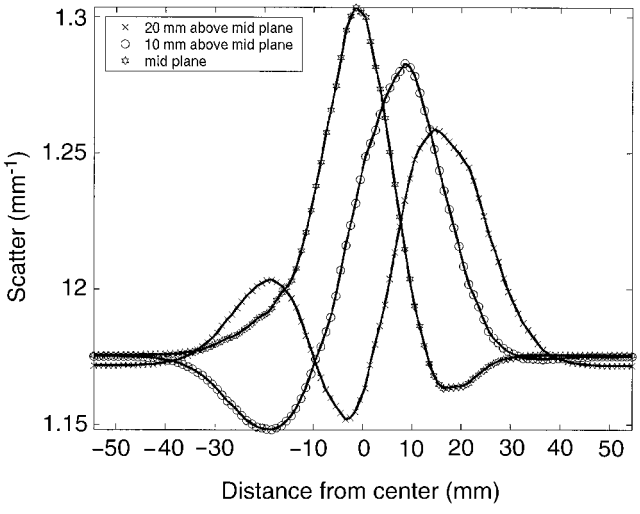

(b)

Fig. 12. Transects of both (a) μ_a and (b) μ_s' at $z = 0$ mm and $y = 0$ mm for images shown in Figs. 4, 10, and 11.

FWHM of the object varies between 16.5 and 18.65 mm for the absorption images and 11.64 and 14.41 mm for the scatter images. Surprisingly, the worst FWHM is seen when the object is near the edge of the phantom, which is due to the boundary artifacts reconstructed within the images. The best FWHM is seen when the anomaly is at a distance of 12–22 mm from the edge, with the scatter images showing the best accuracy when the anomaly is at 17 mm from the edge (FWHM = 11.64 mm).

To assess image reconstruction accuracy when the object does not lie in the middle of the measurement planes, it was necessary to move the anomaly 10 mm above the upper plane of detection fibers at $x = -22$ mm, $y = 0$ mm, and $z = 20$ mm. Data were collected and then the anomaly was moved to $z = 10$ mm (within the topmost plane of measurements) for another set of measurements. Absorption and Scatter 3D images were reconstructed simultaneously from

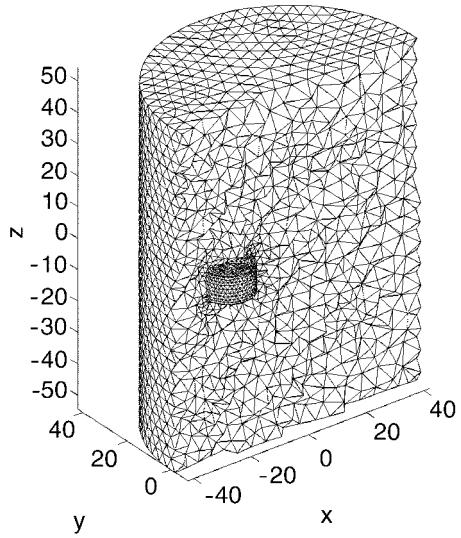

Fig. 13. Finite-element mesh used for modeling and image reconstruction in the case of the incorporating the *a priori* information. As in Fig. 2, the cross section at $y = 0$ mm is shown, to facilitate viewing of the meshing of the anomaly.

these data and shown in Figs. 10 and 11 for $z = 20$ mm and $z = 10$ mm, respectively. The reconstructed images demonstrated that the location of the anomaly was again recovered with good accuracy. Transect plots through the z plane of the model at $x = -22$ and $y = 0$ are shown in Fig. 12(a) and 12(b) and reveal that the peak position of the reconstructed anomaly moves correctly in the z direction as expected. However, the reconstructed images when the anomaly is located at $z = 20$ mm has the greatest error because the photon sampling within that plane is low. Once again the scatter images exhibit better localization accuracy compared with their absorption image counterparts. Furthermore, as evident from the transect plots in Figs. 12(a) and 12(b), there exists a biphasic contrast within these reconstructed images. This contrast is due to the symmetric property of the imaging domain and that of the collected data, i.e., a change in measured data when the anomaly is at $z = 20$ mm could equally be due to a decrease in optical properties at $z = -20$ mm.

Previous studies in two dimensions have shown that objects 8 mm and larger in diameter can be accurately reconstructed and detected for most absorption contrasts that are observed in human tissues, whereas objects as small as 2 mm can be detected with high contrast but cannot be accurately reconstructed.[10] To date, most reported studies in three dimensions have reported poor quantitative accuracy from 3D NIR imaging methods, which is stated to be due to the partial volume effect encountered in three dimensions.[4,13]

Finally, since the reconstructions of the absolute values of optical absorption and scattering were lower than expected, we considered the addition of *a priori* information in our image reconstruction. Here, the exact location and size of the anomaly was

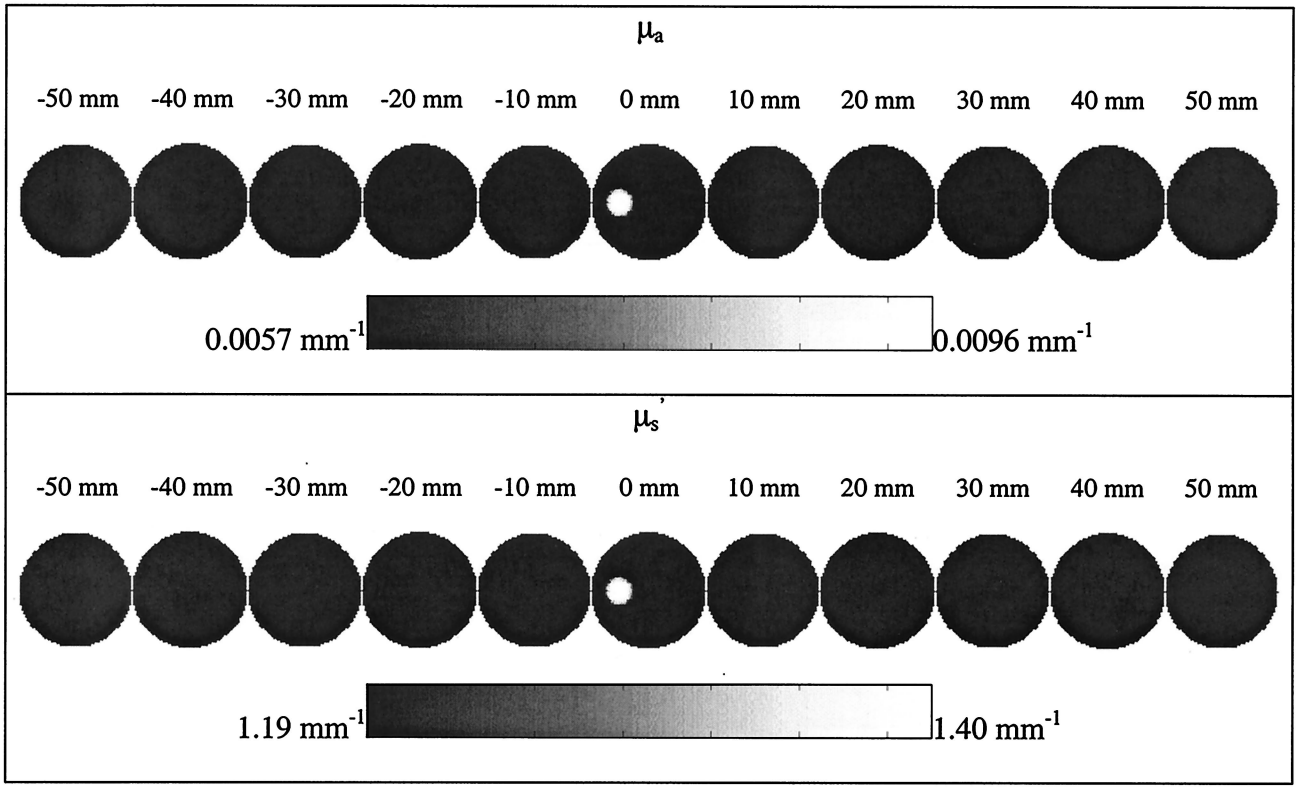

Fig. 14. Reconstructed images when the anomaly is positioned at $x = -22$ mm, $y = 0$ mm, and $z = 20$ mm, and *a priori* information on the position and shape of the anomaly has been included. Top row is absorption images, whereas the bottom row is the reduced scatter images. In each case, images represent 2D cross sections through the reconstructed 3D volume. The right-hand side corresponds to the top of the cylinder ($z = 50$ mm), and the left corresponds to the bottom of the cylinder ($z = -50$ mm), with each slice being a 10-mm increment.

assumed known *a priori*, and this information was used to decrease the number of unknowns in our reconstruction to the two homogenous regions of background and anomaly. With this approach with measured 3D data, we used the reconstruction algorithm to estimate the absolute values of absorption and scatter of the background and the anomaly to within 97% and 93.4%, respectively. This estimation is a significant improvement in the quantitative reconstructed values in 3D NIR optical tomography. Implementation of this type of *a priori* information can be achieved when magnetic resonance imaging (MRI) is combined with NIR and has been shown successfully in 2D image reconstruction of the female breast.[26] As the progression toward full 3D iterative reconstruction in an MRI/NIR imaging system continues, the ability to reconstruct the bulk optical properties of localized regions accurately will become very important.

6. Conclusion

We have investigated the resolution of a small, absorbing and scattering object embedded within a phantom, using a 3D image-reconstruction algorithm. Data were collected from three planes of detectors (16 sources and detectors within each plane) located around a homogenous cylindrical phantom containing a single cylindrical anomaly of radius 8 mm and of height 10 mm. The object was moved both vertically and laterally, and images of absolute absorption and scatter were reconstructed simultaneously for the anomaly when it was positioned at different locations within the phantom. This object represents a challenging test field for NIR imaging, yet is representative of breast cancer tumors, which need to be detected accurately.

It has been shown that by use of multiple planes of measured NIR data and a 3D image reconstruction the location and the size of the anomaly can be calculated with good accuracy. In all cases, the scatter images have exhibited better accuracy compared with the absorption images. The best contrast and resolution was found when the anomaly was near the periphery of the phantom and was positioned within all three planes of measurements.

Recognizing the fact that the quantitative accuracy of these images is poor, we considered the use of *a priori* information within the image-reconstruction algorithm. In this case the size and location of the anomaly was assumed known, and the image-reconstruction algorithm was modified such that only the homogenous optical values within the two regions of the phantom were sought. The accuracy of the quantitative image reconstruction was improved substantially in that it was possible to calculate the absorption and scatter values to within 97% and 93% of

the target, respectively. A key development in this research is the ability to reconstruct fields within the image of varying numbers of nodes, allowing a very flexible way to image either the entire field or the localized regions within the field. This ability illustrates the benefits of structural *a priori* information, which is readily available in a dual-modality MRI–NIR imaging system.

This research has been sponsored by the National Cancer Institute through grants RO1CA69544 and PO1CA80139.

References

1. B. W. Pogue, S. Geimer, T. O. McBride, S. Jiang, U. L. Österberg, and K. D. Paulsen, "Three-dimensional simulation of near-infrared diffusion in tissue: boundary condition and geometry analysis for finite element image reconstruction," Appl. Opt. **40,** 588–600 (2001).
2. H. Dehghani, B. W. Pogue, S. P. Poplack, and K. D. Paulsen, "Multiwavelength three dimensional near infrared tomography of the breast: initial simulation, phantom and clinical results," Appl. Opt. 135–145 (2003).
3. T. O. McBride, B. W. Pogue, S. P. Poplack, S. Soho, W. A. Wells, S. Jiang, U. L. Osterberg, and K. D. Paulsen, "Multi-spectral near-infrared tomography: a case study in compensating for water and lipid content in hemoglobin imaging of the breast," J. Biomed. Opt. **7,** 72–79 (2002).
4. J. C. Hebden, H. Veenstra, H. Dehghani, E. M. C. Hillman, M. Schweiger, S. R. Arridge, and D. T. Delpy, "Three-dimensional time-resolved optical tomography of a conical breast phantom," Appl. Opt. **40,** 3278–3287 (2001).
5. S. Fantini, M. A. Franceschini, E. Gratton, D. Hueber, W. Rosenfeld, D. Maulik, P. G. Stubblefield, and M. R. Stankovic, "Non-invasive optical mapping of the piglet in real time," Opt. Express **4,** 308–314 (1999).
6. H. Eda, I. Oda, Y. Ito, Y. Wada, Y. Oikawa, Y. Tsunazawa, Y. Tsuchiya, Y. Yamashita, M. Oda, A. Sassaroli, Y. Yamada, and M. Tamaru, "Multichannel time-resolved optical tomographic imaging system," Rev. Sci. Instrum. **70,** 3595–3602 (1999).
7. D. A. Boas, D. H. Brooks, E. L. Miller, C. A. DiMarzio, M. Kilmer, R. J. Gaudette, and Q. Zhang, "Imaging the body with diffuse optical tomography," IEEE Signal Process. Mag. **18,** 57–75 (2001).
8. S. R. Arridge, "Optical tomography in medical imaging," Inverse Probl. **15,** R41–R93 (1999).
9. H. Jiang, K. D. Paulsen, U. L. Osterberg, and M. Patterson, "Frequency domain optical image reconstruction in turbid media: an experimental study of single-target delectability," Appl. Opt. **36,** 52–63 (1997).
10. B. W. Pogue, C. Willscher, T. McBride, U. L. Osterberg, and K. D. Paulsen, "Contrast-detail analysis for detection and characterization with near-infrared diffuse tomography," Med. Phys. **27,** 2693–2700 (2000).
11. M. Schweiger and S. R. Arridge, "Comparison of two- and three-dimensional reconstruction methods in optical tomography," Appl. Opt. **37,** 7419–7428 (1998).
12. H. Jiang, Y. Xu, N. Iftimia, J. Eggert, K. Klove, L. Baron, and L. Fajardo, "Three-dimensional optical tomographic imaging of breast in a human subject," IEEE Trans. Med. Imaging **20,** 1334–1340 (2001).
13. A. Gibson, R. M. Yusof, E. M. C. Hillman, H. Dehghani, J. Riley, N. Everdale, R. Richards, J. C. Hebden, M. Schweiger, S. R. Arridge, and D. T. Delpy, "Optical tomography of a realistic neonatal head phantom," Appl. Opt. **42,** 3109–3116 (2003).
14. B. W. Pogue, X. Song, T. D. Tosteson, T. O. McBride, S. Jiang, and K. D. Paulsen, "Statistical analysis of non-linearlly reconstructed near-infrared tomographic images: Part I - theory and simulation," IEEE Trans. Med. Imaging **21,** 755–763 (2002).
15. X. Song, B. W. Pogue, T. D. Tosteson, T. O. McBride, S. Jiang, and K. D. Paulsen, "Statistical analysis of nonlinearly reconstructed near-infrared tomographic images: Part II - experimental interpretation," IEEE Trans. Med. Imaging **21,** 764–772 (2002).
16. T. O. McBride, "Spectroscopic reconstructed near infrared tomographic imaging for breast cancer diagnosis," Ph.D. dissertation (Dartmouth College, Hanover, N.H., 2001).
17. M. J. Eppstein, D. J. Hawrysz, A. Godavarty, and E. M. Sevick-Muraca, "Three-dimensional, Baysian image reconstruction from sparse and noisy data sets: near-infrared fluorescence tomography," Proc. Natl. Acad. Sci. USA **99,** 9619–9624 (2002).
18. M. Schweiger, S. R. Arridge, M. Hiroaka, and D. T. Delpy, "The finite element model for the propagation of light in scattering media: boundary and source conditions," Med. Phys. **22,** 1779–1792 (1995).
19. H. Jiang, K. D. Paulsen, U. L. Osterberg, B. W. Pogue, and M. S. Patterson, "Optical image reconstruction using frequency-domain data: simulations and experiments," J. Opt. Soc. Am. A **13,** 253–266 (1996).
20. S. R. Arridge, M. Schweiger, M. Hiraoka, and D. T. Delpy, "A finite element approach for modeling photon transport in tissue," Med. Phys. **20,** 299–309 (1993).
21. K. D. Paulsen and H. Jiang, "Spatially varying optical property reconstruction using a finite element diffusion equation approximation," Med. Phys. **22,** 691–701 (1995).
22. S. R. Arridge and M. Schweiger, "Photon-measurement density functions. Part 2: Finite-element-method calculations," Appl. Opt. **34,** 8026–8037 (1995).
23. R. Penrose, "A generalized inverse for matrices," Proc. Cambridge Philos. Soc. **51,** 406–413 (1955).
24. J. Schoberl, "NETGEN—an automatic 3D tetrahedral mesh generator," http://www.sfb013.uni-linz.ac.at/~joachim/netgen/.
25. M. Schweiger and S. R. Arridge, "Optical tomographic reconstruction in a complex head model using a priori region boundary information," Phys. Med. Biol. **44,** 2703–2722 (1999).
26. V. Ntziachristos, A. G. Yodh, M. Schnall, and B. Chance, "Concurrent MRI and diffuse optical tomography of breast following Indocyanine Green enhancement," Proc. Natl. Acad. Sci. USA **97,** 2767–2772 (2000).